Energy Technology & Environmental Science

Dense MoS_2 Micro-Flowers Planting on Biomass-Derived Carbon Fiber Network for Multifunctional Sulfur Cathodes

Rameez Razaq,[a, b, c] Nana Zhang,[b] Ying Xin,[b] Qian Li,[b] Jin Wang,[b] and Zhaoliang Zhang*[a, b]

The significant challenge in lithium-sulfur batteries (LSBs) arises from low conductivity of sulfur cathode, loss of active sulfur species due to less anchoring sites and sluggish redox kinetics of lithium polysulfides (LPSs). Herein, the dense MoS_2 micro-flowers assembled by cross-linked 2D MoS_2 nanoflakes planting on biomass-derived carbon fiber (CF) network (MoS_2/CFs) are fabricated as multifunctional sulfur cathodes of LSBs. The 2D MoS_2 nanoflakes supported on CF provide abundant anchoring sites for strong adsorption, while the 3D flowerlike structure prevents lamellar aggregation of 2D MoS_2 nanoflakes. Importantly, the dense MoS_2 micro-flowers planting on the network weaved by biomass-derived CFs ensures the high electronic conductivity of the MoS_2/CFs composite, sufficient electrode/electrolyte interaction, fast electron and Li^+ transportation. Moreover, the CF network weaved from cost-effective tissue paper reduces the cost of LSBs. Thus, the S-MoS_2/CFs cathode exhibits a high rate capability (1149 and 608 mA h g^{-1} are obtained at 0.2 C and 4 C, respectively), excellent cyclic performance with ~75% capacity retention and 99% Coulombic efficiency at 2 C after 500 cycles, corresponding to ~0.05% capacity fading per cycle only, as well as structure integrity during the discharge/charge process.

Introduction

Lithium-sulfur batteries (LSBs) have gained immense consideration in the practical applications of electric vehicles, satellites, and other portable energy-storage devices due to their high theoretical energy density of 2600 Wh kg^{-1}.[1] However, their practical application is still hampered by three core hurdles.[2] First, the insulating nature of orthorhombic sulfur with a very low conductivity of only 5×10^{-28} S m^{-1} which impedes the sulfur utilization and decreases the rate capability of LSBs. Second, the notorious "shuttling of the LPSs" caused by dissolution and diffusion of intermediate polysulfides which reduces the discharge/charge capacity and causes the sluggish redox kinetics. Third, the unstable structure of the cathode due to massive volume change may disfigure the structure of cathodes and worsen the cycling performance of LSBs.[3] Fortunately, these key challenges can be minimized by rational design of multifunctional conductive macro-/nan o-/micro-structured composite cathodes.

Till now, these composites fall into three categories. The first is conductive carbon, such as microporous carbon,[4] mesoporous carbon,[5] carbon fibers (CFs),[6] carbon sphere,[7] carbon nanotubes,[8,9] and CF cloth.[10] Owing to their electrically conductive pathways, these carbon materials serve as a physical barrier to confine the lithium polysulfides (LPSs). However, the physical confinement is not sufficient to trap LPSs. Over a long cycle life, sulfur species detached form nonpolar carbon are suspected to result in loss of active materials, increase of the charge transfer resistance, accumulation of insulating layers on the anode, and finally severe capacity fading.

Doped carbon with anchoring sites and effective electron pathway is designated as the second category. To provide anchoring sites for chemical adsorption of LPSs intermediates, the introduction of polar sites onto conductive carbon materials have been reported. For instance, graphene oxides,[11] B and O-doped CNT,[12] N-doped graphene/CNT,[13] B-doped graphene,[14] N-doped hollow carbon spheres,[15] P, N-codoped carbon nanospheres,[16] and N or O-codoped carbon[17] have been widely explored for LSBs. The carbon materials contribute the conductive framework, while the doped sites on the conductive carbons enhance the chemical anchoring. However, the contents of doping atoms are not enough to control the flood of LPSs.

To further enhance the binding with LPSs, the third category, namely, polar and conductive transition metal compounds collaborated with carbon materials, such as transitional metal oxides,[18,19] carbides,[20] nitrides,[21–23] sulfides[24–27] and porphyrin,[28] have emerged to chemically adsorb LPSs. Generally, most of the previously reported transition metal

[a] Dr. R. Razaq, Prof. Z. Zhang
Institute of Catalysis for Energy and Environment, College of Chemistry and Chemical Engineering
Shenyang Normal University
Shenyang 110034, Liaoning, China
E-mail: chm_zhangzl@ujn.edu.cn
[b] Dr. R. Razaq, N. Zhang, Dr. Y. Xin, Dr. Q. Li, Dr. J. Wang, Prof. Z. Zhang
School of Chemistry and Chemical Engineering, Shandong Provincial Key Laboratory of Fluorine Chemistry and Chemical Materials
University of Jinan
Jinan, 250022, Shandong, China
[c] Dr. R. Razaq
University of Michigan-Shanghai Jiao Tong University Joint Institute
Shanghai JiaoTong University

Supporting information for this article is available on the WWW under https://doi.org/10.1002/slct.202001729

composites are either micro-sized or bulk materials, restricting available anchoring sites towards LPSs.[29] Recently, two dimensional (2D) layered transition metal dichalcogenides (TMDs) are attractive due to large exposed active surfaces for sulfur coverage and conversion.[30] 2D MoS_2 is a typical member in the family of TMDs.[31] Nevertheless, 2D MoS_2 nanosheets suffer from easy aggregation and limited conductivity. The former can be efficiently overcome by the hierarchical assembly of 2D nanosheets into 3 dimensional (3D) configurations[32] and the latter is always solved by rationally coupling with carbon materials, for example, carbon nanotube and/or graphene.[33]

Herein, we designed and fabricated dense MoS_2 micro-flowers assembled by cross-linked 2D MoS_2 nanoflakes planting on biomass-derived CF network (MoS_2/CFs) for multifunctional sulfur cathodes of LSBs. The 2D MoS_2 nanoflakes provide abundant anchoring sites for strong adsorption and redox conversion of LPSs, while the 3D flowerlike structure prevents lamellar aggregation of 2D MoS_2 nanoflakes. Importantly, the dense MoS_2 micro-flowers planting on the network weaved by biomass-derived CFs ensures the high electronic conductivity of the MoS_2/CFs composite, sufficient electrode/electrolyte interaction, fast electron and Li^+ transportation. Moreover, the large-scale production of biomass-derived conductive CFs from cost-effective tissue paper reduces the cost of LSBs. Thus, the S-MoS_2/CFs cathode achieves high sulfur retention and conversion as well as excellent electrochemical performance.

Results and Discussion

Scheme 1 depicts the synthesis procedure of the MoS_2/CFs. Commercial tissue paper interwoven by cellulose fibers is used as the growth substrate after purifying with 1 M HCl. The purified tissue paper is immersed into a solution containing thiourea and ammonium molybdate tetrahydrate. Then, the slurry is hydrothermally treated at 180 °C for 24 h. After filtration and washing, the precipitate is calcined at 800 °C in Ar in order to transform the tissue paper into CFs. The as-obtained MoS_2/CFs was loaded with sulfur by vapor phase infusion method.

The carbonized tissue paper was first examined by Field emission scanning electron microscopy (FESEM) equipped with energy dispersive spectroscopy (EDS) and X-ray diffraction (XRD) (Figure S1), demonstrating the interwoven 3D network of CFs. Then, the XRD pattern confirmed the presence of the 2H-type MoS_2 phase (JCPDS 37–1492) for MoS_2/CFs (Figure 1a). Furthermore, the FESEM images of MoS_2/CFs show uniform and densely packed MoS_2 flowers at a large scale on CFs (Figure 1b, c). Specifically, the low-magnification FESEM image shows that CFs retain the interwoven structure after supporting MoS_2 flowers (Figure 1b). The interstitial area between CFs is useful for the penetration of electrolyte, thereby smoothing the redox conversion of LPSs. The high-magnification FESEM images of MoS_2/CFs show that the MoS_2 flowers consist of petals of thin 2D nanoflakes with a thickness of ~10 nm, which all radiate from the center and cross-link together (Figure 1c, d). The unique 3D structure of MoS_2 flowers with numerous nanoflakes and nanovoids, not only hinders the 2D nanoflakes to entangle and restack but also brings efficient electron transfer due to linkage through CF networks. The Transmission electron microscopy (TEM) images of the MoS_2 nanoflakes demonstrate an interlayer spacing of 0.62 nm, corresponding to (002) plane of MoS_2 (Figure. 1e, f), consistent with the XRD result. The content of MoS_2 in the MoS_2/CFs composite obtained by EDS is estimated to be ~76 wt% (Figure S2).

The as-obtained MoS_2/CFs composite are further evaluated by N_2 adsorption/desorption isotherm measurement. The Brunauer–Emmett–Teller (BET) specifc surface area and pore volume are calculated to be 22.6 m^2/g and 0.027 cm^3/g, respectively (Figure S3).

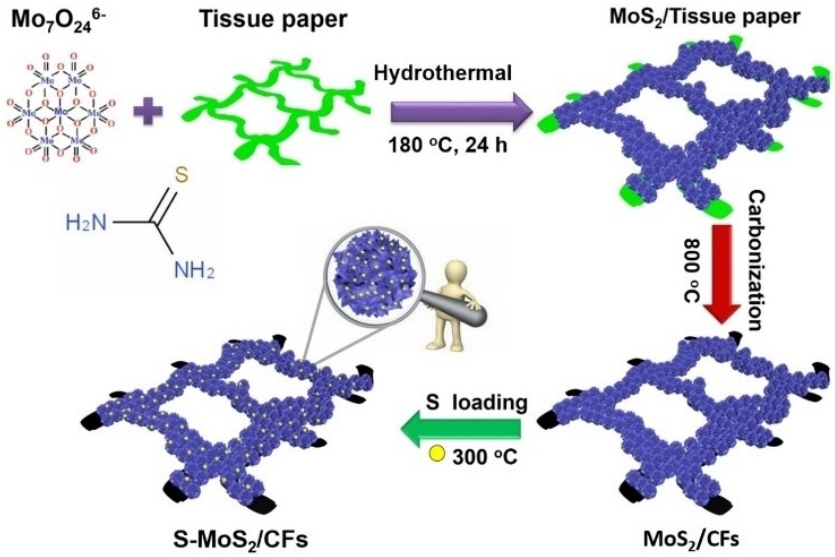

Scheme 1. Illustration for the preparation of MoS_2/CFs and the sulfur loading using vapor phase infusion method.

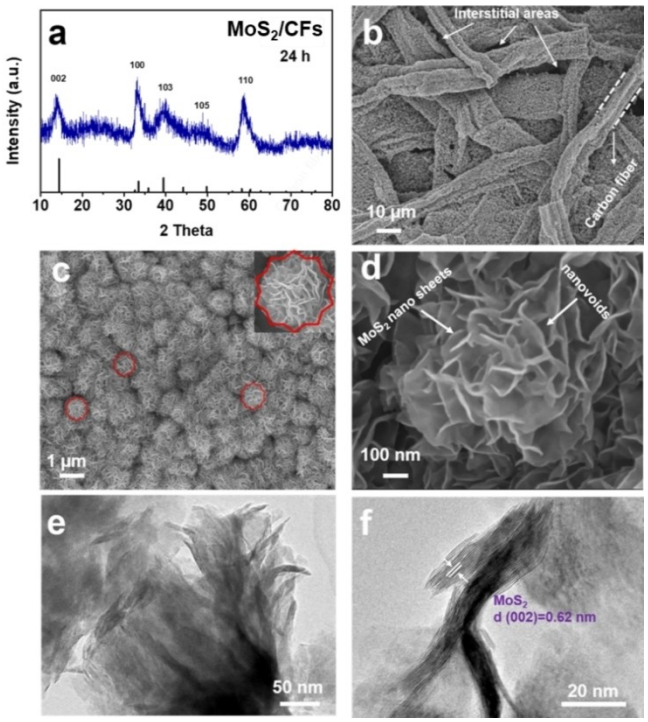

Figure 1. XRD pattern (a), FESEM images (b-d) and TEM images (e, f) of MoS_2/CFs.

X-ray photoelectron spectroscopy (XPS) survey shows the element composition of C, Mo, S and O in MoS_2/CFs (Figure 2a). The high-resolution XPS spectra of C, Mo and S were further recorded (Figure 2b-d). From C 1s spectrum (Figure 2b), the C–C/C=C, C–O and C=O groups were observed at binding energies of 284.1, 286.3 and 288.6 eV,[34] respectively. As expected, the Mo 3d spectrum shows characteristic +4 oxidation state[31] (Figure 2c), corresponding to the assignment of the S 2p spectrum to sulfide ions (S^{2-})[31] (Figure 2d), confirming the MoS_2 surface.

The FESEM images show that the S-MoS_2/CFs composite well maintains the original morphology (Figure 3a, b), suggesting that no extra sulfur exists outside the MoS_2/CFs structure. However, the composites after sulfur loading by both melt diffusion method[19] (Figure S4a) and *in situ* oxidation method[26] (Figure S4b) present sever aggregates of sulfur. EDX mappings of S-MoS_2/CFs show that sulfur is homogeneously distributed on the MoS_2/CFs host (Figure 3c-f), indicating that sulfur has been successfully accommodated and immobilized on the surface and within the voids of MoS_2/CFs. XRD confirms the presence of sulfur (S_8, JCPDS 08–0247) (Figure 3g). The sulfur loading in S-MoS_2/CFs is determined by thermo-gravimetry analysis (TGA) to be 72 wt.% (Figure 3h). As a control sample, S-CFs was also prepared by vapor phase infusion method (Figure S5), and TGA gives 66 wt.% sulfur loading (Figure S6).

The electrochemical performances of the S-MoS_2/CFs and S-CFs cathodes were measured by fabricating 2025-type coin cells. Figure 4a shows the cyclic performance of S-MoS_2/CFs and S-CFs at 0.5 C. The S-MoS_2/CFs electrode exhibits the discharge capacity of 1033.9 mAh g^{-1} with 88% capacity retention after 100 cycles. Furthermore, the Coulombic efficiency is ~100%. By sharp contrast, S-CFs shows low discharge capacity with low capacity retention (78%) after 100 cycles. Moreover, the discharge/charge plateau of S-MoS_2/CFs shows a less hysteresis (△E = 0.18 V) compared with that of S–C (△E = 0.26 V) (Figure 4b), suggesting the improved electrochemical kinetics of LPSs conversion on MoS_2/CFs. At a current density of

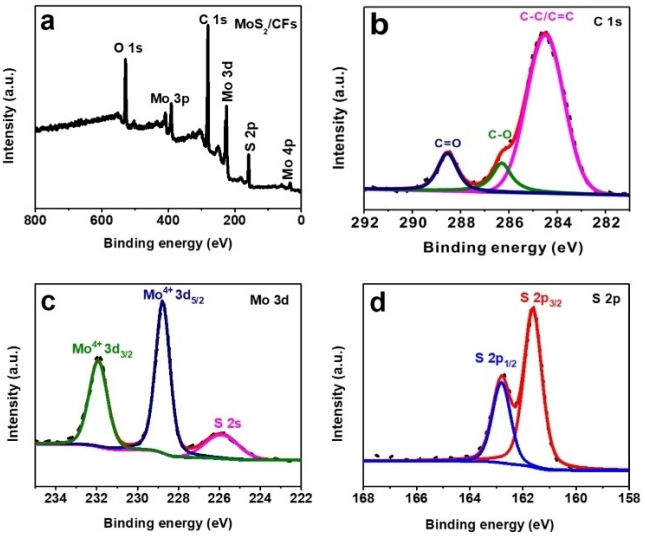

Figure 2. XPS spectra (a), high-resolution XPS spectra of C 1s (b) Mo 3d (c), and S 2p (d) of MoS_2/CFs.

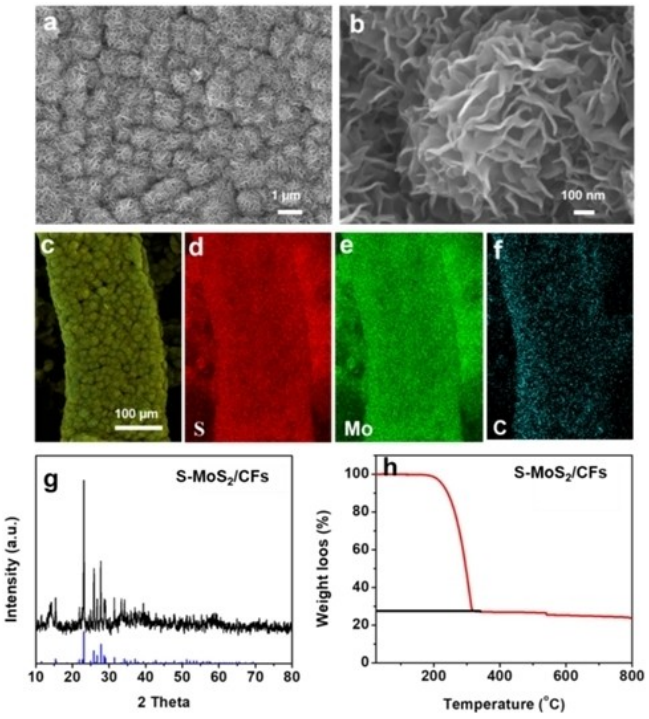

Figure 3. FESEM images and elemental mappings (a-f), XRD pattern (g)

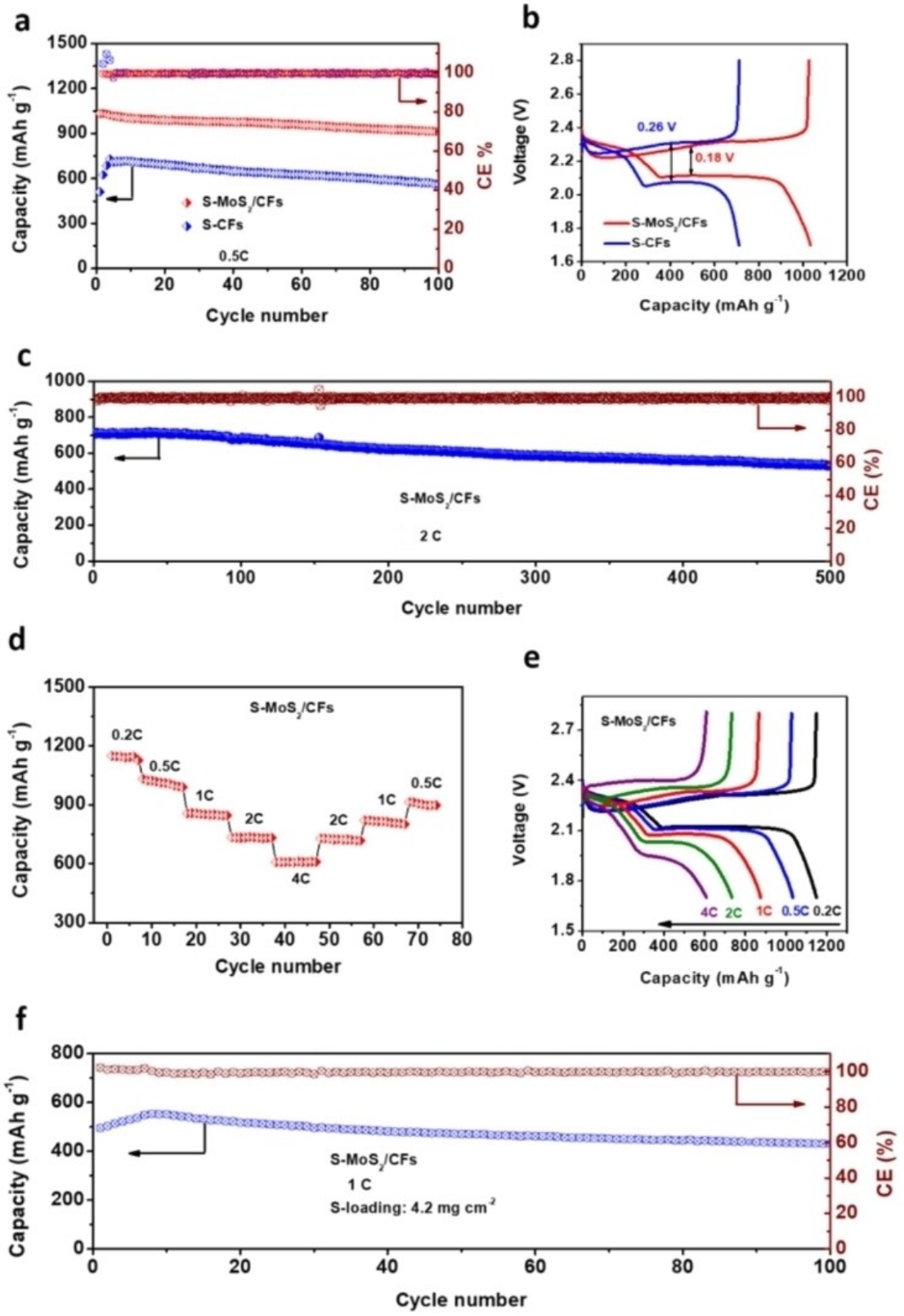

Figure 4. Cycling performance and Coulombic efficiency for the S-MoS_2/CFs and S-CFs cathodes at 0.5 C over 100 cycles (a), galvanostatic discharge/charge curves for the S-MoS_2/CFs and S-CFs cathodes at 0.5 C (b), Long cyclic performance and Coulombic efficiency for S-MoS_2/CFs at 2 C for 500 cycles (c), Rate performance (d), and Galvanostatic discharge/charge curves of the S-Mo_2C/HCFs cathode at different current densities (e), Cycling performance and Coulombic efficiency of S-MoS_2/CFs at 4.2 mg cm^{-2} areal sulfur loading and 100 cycles (f)

2 C, the specific capacity can reach up to 714 and retain ~533 mAh g^{-1} (with ~75% retention) after 500 cycles with 99% Coulombic efficiency, corresponding to ~0.05% capacity fading per cycle only (Figure 4c).

Figure 4d shows the rate performance of S-MoS_2/CFs. The specific capacities at the current densities of 0.2 C, 0.5 C, 1 C, 2 C, and 4 C are 1149, 1027, 856, 723, and 608 mA h g^{-1}, respectively. Evidently, good capacity reversibility (913 mA h g^{-1}) is achieved at 0.5 C. Figure 4e shows the galvanostatic discharge/charge profiles of S-MoS_2/CFs at C-rates of 0.2 C to 4 C. The typical multi-step reduction reactions with two reaction plateaus can be observed in the discharge process. The upper reduction plateau comprises of reduction of sulfur into long-chain LPSs, and the lower plateau is assigned to the subsequent formation of short-chain LPSs to Li_2S, whereas the charge plateau corresponds to the transformation of Li_2S_2/Li_2S to Li_2S_8/S_8. Importantly, the galvanostatic discharge/charge voltage profile of S-MoS_2/CFs at 4 C is still obvious.

The thick electrode with high areal sulfur loading is crucially important for practical LSBs.[35] The cyclic performance of S-MoS_2/CFs with a high sulfur loading of 4.2 mg cm^{-2} was further investigated at 1 C (Figure 4f). The S-MoS_2/CFs cathode shows high discharge capacity of 553 mAh g^{-1} at 1 C corresponds to 85% capacity retention over 100 cycles. Furthermore, the corresponding Coulombic efficiency is stabilized around 99% after 100 cycles.

The excellent electrochemical performance is supposed from the multifunctional effects of MoS_2/CFs. First, the LPSs adsorption experiments were performed. MoS_2/CFs and CFs are dispersed separately into the pristine Li_2S_4 solution with stirring for 30 min and left undisturbed for 12 h. As observed in Figure 5a, a distinctive change in color was observed for MoS_2/CFs, indicating the stronger trapping ability of MoS_2/CFs for LPSs in comparison with CFs.

Secondly, cyclic voltammetry (CV) tests were performed for symmetric cells within a voltage range of −0.7 to +0.7 V[25] (Figure 5b). The increased current density of MoS_2/CFs over CFs demonstrates the enhanced kinetics of the redox reactions and the reduced overpotential for LPSs conversion, which is direct evidence of polysulfide electrocatalysis on MoS_2/CFs.[23,36] Furthermore, electrochemical impedance spectroscopy (EIS) measured on symmetric cells reveals a low charge transfer resistance (R_{ct}) for MoS_2/CFs (Figure 5c), which is another evidence of the electrocatalytic effects derived from the unique 3D architecture of uniformly dispersed MoS_2 flowers interconnected with CF

Thirdly, Li^+ ion diffusion is often a bottleneck during the electrochemical reaction process in LSBs. CV curves for S-MoS_2/CFs (Figure S7) and S-CFs (Figure S8) were performed at different scan rates, which exhibit two cathodic peaks (I and II) and one anodic peak (III). Note that the cathodic peak I at low scan rates (0.1 and 0.2 mV s^{-1}) for S-CFs is discerned two peaks, maybe due to two types of anchoring sites based on XPS, such as C–C/C=C and C=O/C–O species (Figure 2b). However, no split was observed for S-MoS_2/CFs, because the dense coverage of CFs by 3D MoS_2 flowers minimized the contact between CFs and electrolyte, which depressed the absorption and conversion of LPSs on CFs.[37] Furthermore, the high current density

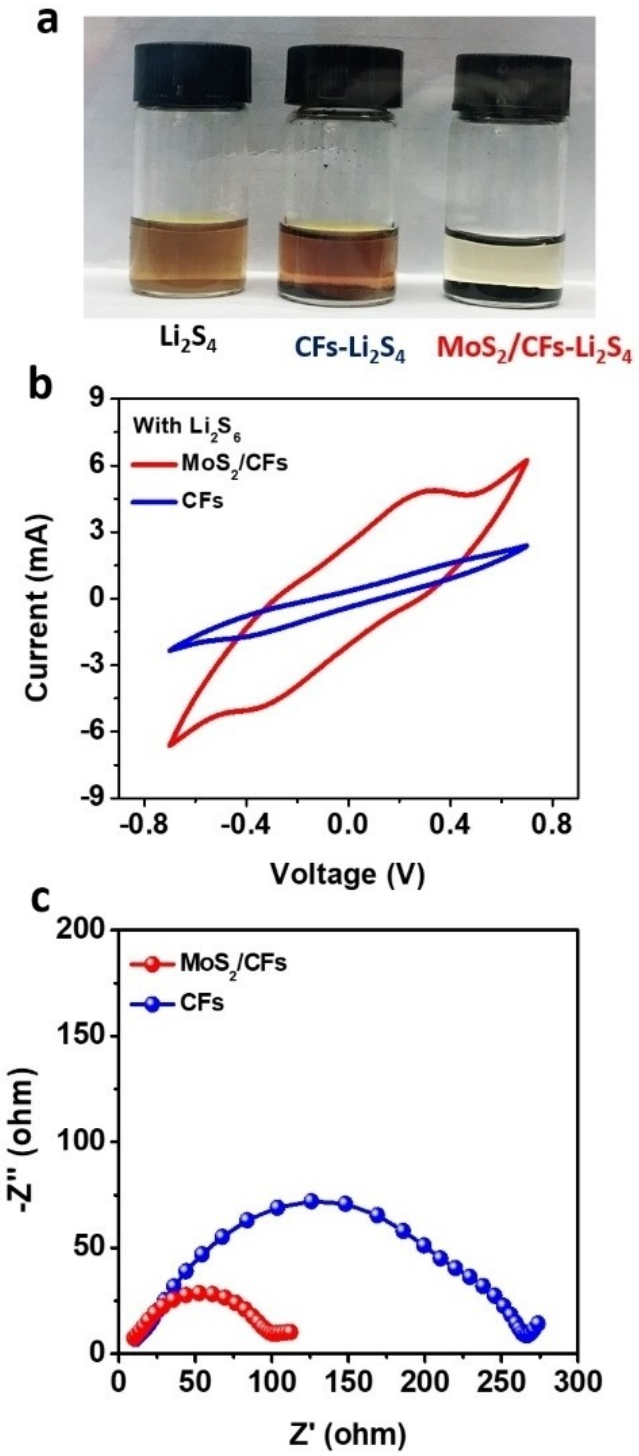

Figure 5. Visualized adsorption of Li_2S_4 on MoS_2/CFs and CFs (a), Polarization curves (b) and EIS spectra (c) of symmetrical cells for MoS_2/CFs and CFs.

for S-MoS_2/CFs suggests that the cell polarization decreases and the participation of active materials on redox reactions increases, consistent with discharge/charge profiles. In addition, as the scan rates increase, the S-MoS_2/CFs electrode displays a less decrease in onset potentials for peaks I, II, and III (Figure. 6a, b) than S-CFs (Figure 6c, d), demonstrating the accelerated

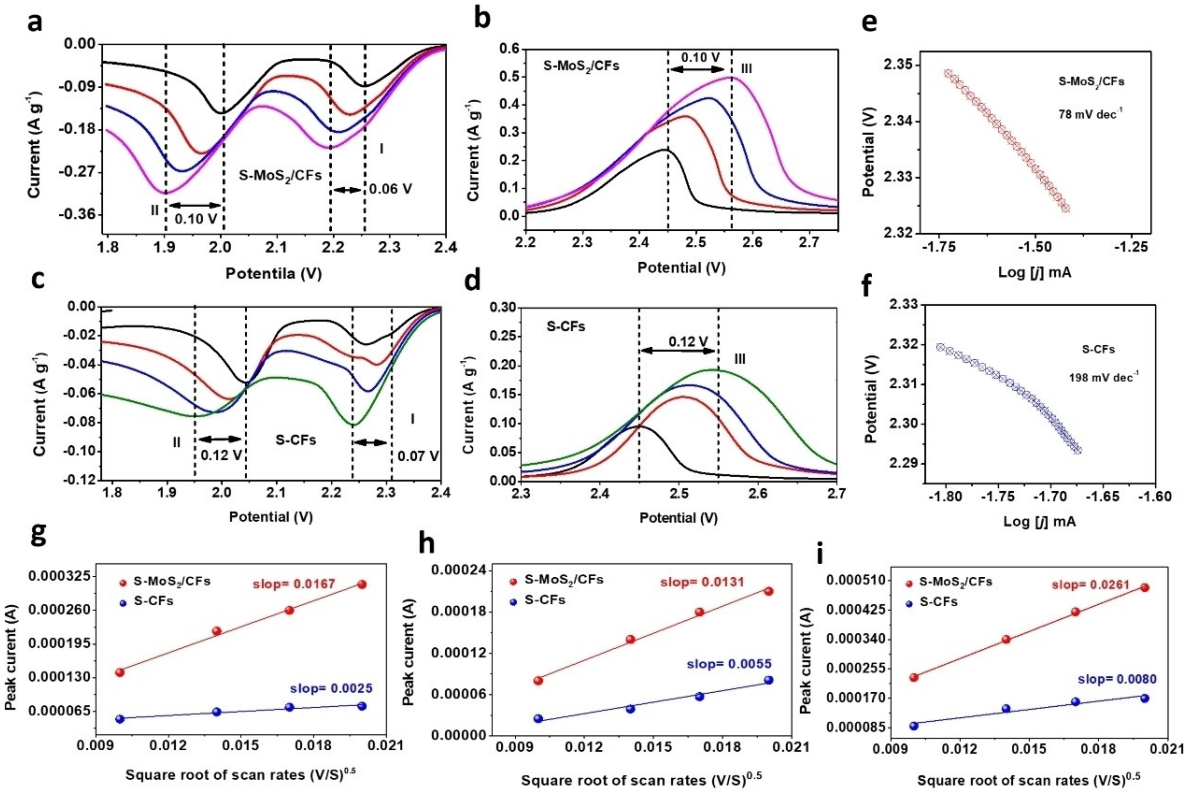

Figure 6. The CV data of MoS_2/CFs (a, b) and S-CFs (c, d) at different scan rates. Tafel plots of MoS_2/CFs (e) and S-CFs (f). Plots of peak currents versus the square root of scan rates for MoS_2/CFs and S-CFs: the cathodic reaction I (S_8-Li_2S_4) (g), the cathodic reaction II (Li_2S_4-Li_2S) (h), and the anodic reaction III (Li_2S-S_8) (i)

redox conversion of LPSs on MoS_2/CFs.[22,38] The electrocatalytic effect was also analyzed by Tafel slope using the CV curve at 0.1 mV s^{-1}. S-MoS_2/CFs displays Tafel slope of 78 mV dec^{-1} (Figure 6e), much smaller than that of S-CFs (198 mV dec^{-1}) (Figure 6f), suggesting the enhanced redox kinetics of LPSs over S-MoS_2/CFs.[39,40]

The Li^+ diffusion was explored under different scanning rates ranging from 0.1 to 0.4 mV s^{-1}. As shown in Figure 6g-i, all cathodic and anodic peak currents are linear with the square root of scan rates, from which the Li^+ diffusion rate can be estimated using the classical Randles Sevcik equation:[41]

$$I_p = (2.69 \times 10^5)\, n^{1.5}\, S\, D_{Li}^{0.5}\, C_{Li}\, \nu^{0.5}$$

Where I_p is the peak current, n is the charge transfer number, S is the surface area of the electrode, D_{Li} is the Li^+ diffusion coefficient, C_{Li} is Li^+ concentration, and ν is the scan rate. Because n, S, and C_{Li} are unchanged, the slope of the line ($I_p/\nu^{0.5}$) represents the Li^+ diffusion rate. As observed in Fig. 6 g-i, the Li^+ diffusion rate is higher for S-MoS_2/CFs compared with S-CFs. The enhanced Li^+ diffusion further promotes the catalytic effect of MoS_2/CFs, which is a critical factor determining the battery performance.

Figure 7a schematically illustrates the LPSs adsorption, electrocatalytic electron and Li^+ transfer effects. The unique 3D MoS_2 flowers provide numerous nanoflakes and nanovoids for polysulfides retention and electrocatalytic conversion as well as

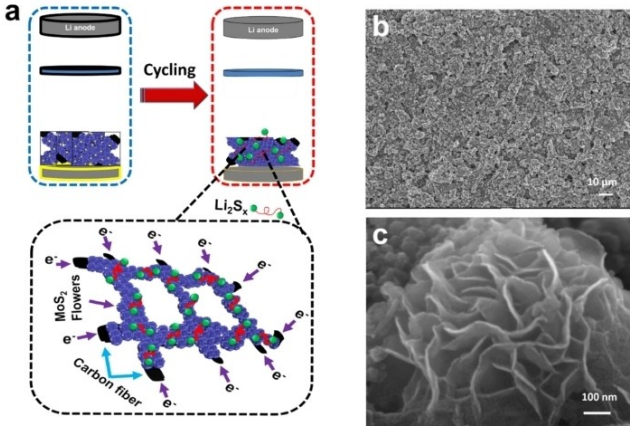

Figure 7. Schematic illustration of the mechanisms during redox reactions (a), FESEM images of MoS_2/CFs after cycling (b, c).

Li^+ diffusion. Simultaneously, electrons can be effectively collected and transferred to CFs. To further validate the superiority of S-MoS_2/CFs after long cycling, the cells are disassembled at fully charging state. FESEM shows that the morphology of the S-MoS_2/CFs cathode is well maintained after cycling (Figure 7b, c), confirming mechanical robustness of MoS_2/CFs. Just recently, Qiao and co-authors proposed that the practical route for Li–S battery commercialization is fabrication of 3D electrodes from 2D sulfides to take full advantage of their

multiple functions.[42] Here, the developed MoS_2/CFs is the right choice to meet this requirement. Compared with similar systems published in top journals (Table S1), S-MoS_2/CFs outperforms in terms of initial capacity, capacity retention and Coulombic efficiency in the state of the art LSBs batteries.

Conclusion

In summary, the dense MoS2 micro-flowers assembled by cross-linked 2D MoS2 nanoflakes planting on biomass-derived CF network (MoS2/CFs) are fabricated as sulfur cathodes of LSBs. The specific architecture possesses multiple functions: (i) prevents lamellar aggregation of 2D nanoflakes; (ii) minimizes the interface between CFs and the electrolyte; (iii) supplies abundant anchoring sites for adsorption and catalytic conversion of LPSs; (iv) enables sufficient electrode/electrolyte interaction and fast electron transfer; (v) promotes the Li + ion transportation. Furthermore, the CF network derived from tissue paper is cost-effective. Thus, the S-MoS2/CFs cathode exhibits a high rate capability (1149 and 608 mA h g-1 are obtained at 0.2 C and 4 C, respectively) and excellent cyclic performance with ~75% capacity retention and 99% Coulombic efficiency at 2 C after 500 cycles, corresponding to ~0.05% capacity fading per cycle only. Remarkably, the structural integrity of the MoS_2 flowers is still preserved even after long cycling.

Supporting Information Summary

Sample synthesis, sample characterization and electrochemical measurements are given in detail in supporting information.

Acknowledgements

This work was supported by LiaoNing Revitalization Talents Program (No. XLYC1802076) and National Natural Science Foundation of China (No. 21876061, 21906063 and 21805112).

Conflict of Interest

The authors declare no conflict of interest.

Keywords: Biomass-derived carbon fiber network · Dense MoS_2 micro-flower · Lithium · Polysulfide adsorption · Redox chemistry

[1] Q. Pang, X. Liang, C. Y. Kwok, L. F. Nazar, *Nat. Energy* **2016**, *1*,16132.
[2] J. He, A. Manthiram, *Energy Storage Mater.* **2019**, *20*, 55–70.
[3] a) A. Manthiram, Y. Fu, S. H. Chung, C. Zu, Y. S. Su, *Chem. Rev.* **2014**, *114*, 11751–11787; b) X. Liu, J. Q. Huang, Q. Zhang, L. Mai, *Adv. Mater.* **2017**, *29*, 1601795.
[4] Z. Li, L. Yuan, Z. Yi, Y. Sun, Y. Liu, Y. Jiang, Y. Shen, Y. Xin, Z. Zhang, Y. Huang, *Adv. Energy Mater.* **2014**, *4*, 1301473.
[5] D. Li, F. Han, S. Wang, F. Cheng, Q. Sun, W. C. Li, *ACS Appl. Mater. Interfaces* **2013**, *5*, 2208–2213.
[6] G. Zheng, Q. Zhang, J. J. Cha, Y. Yang, W. Li, Z. W. Seh, Y. Cui, *Nano Lett.* **2013**, *13*, 1265–1270.
[7] N. Jayaprakash, J. Shen, S. S. Moganty, A. Corona, L. A. Archer, *Angew. Chem. Int. Ed.* **2011**, *50*, 5904–5908; *Angew. Chem.* **2011**, *123*, 6026–6030.
[8] X.-B. Cheng, J.-Q. Huang, Q. Zhang, H.-J. Peng, M.-Q. Zhao, F. Wei, *Nano Energy* **2014**, *4*, 65–72.
[9] L. Wang, Z. Yang, H. Nie, C. Gu, W. Hua, X. Xu, X. a Chen, Y. Chen, S. Huang, *J. Mater. Chem. A* **2016**, *4*, 15343–15352.
[10] R. Elazari, G. Salitra, A. Garsuch, A. Panchenko, D. Aurbach, *Adv. Mater.* **2011**, *23*, 5641–5644.
[11] L. Ji, M. Rao, H. Zheng, L. Zhang, Y. Li, W. Duan, J. Guo, E. J. Cairns, Y. Zhang, *J. Am. Chem. Soc.* **2011**, *133*, 18522–18525.
[12] C. Jin, W. Zhang, Z. Zhuang, J. Wang, H. Huang, Y. Gan, Y. Xia, C. Liang, J. Zhang, X. Tao, *J. Mater. Chem. A* **2017**, *5*, 632–640.
[13] D. Su, M. Cortie, G. Wang, *Adv. Energy Mater.* **2017**, *7*, 1602014.
[14] P. Shi, Y. Wang, X. Liang, Y. Sun, S. Cheng, C. Chen, H. Xiang, *ACS Sustainable Chem. Eng.* **2018**, *6*, 9661–9670.
[15] W. Zhou, X. Xiao, M. Cai, L. Yang, *Nano Lett.* **2014**, *14*, 5250–5256.
[16] J. Wang, H. Yang, Z. Chen, L. Zhang, J. Liu, P. Liang, H. Yang, X. Shen, Z. X. Shen, *Adv. Sci.* **2018**, *5*, 1800621.
[17] M. Chen, S. Jiang, S. Cai, X. Wang, K. Xiang, Z. Ma, P. Song, A. C. Fisher, *Chem. Engineering J.* **2017**, *313*, 404.
[18] a) H. Wang, T. Zhou, D. Li, H. Gao, G. Gao, A. Du, H. Liu, Z. Guo, *ACS Appl. Mater. Interfaces* **2017**, *9*, 4320–4325; b) Z. Li, J. Zhang, B. Guan, D. Wang, L.-M. Liu, X. W. Lou, *Nat. Commun.* **2016**, *7*, 13065; c) S. Imtiaz, Z. A. Zafar, R. Razaq, D. Sun, Y. Xin, Q. Li, Z. Zhang, L. Zheng, Y. Huang, J. A. Anderson, *Adv. Mater. Interfaces* **2018**, *5*, 1800243.
[19] R. Razaq, D. Sun, Y. Xin, Q. Li, T. Huang, Z. Zhang, Y. Huang, *Adv. Mater. Interfaces* **2019**, *6*, 1801636.
[20] a) B. Cao, Y. Chen, D. Li, L. Yin, Y. Mo, *ChemSusChem* **2016**, *9*, 3338–3344; b) W. Bao, D. Su, W. Zhang, X. Guo, G. Wang, *Adv. Funct. Mater.* **2016**, *20*, 8746–4756; c) R. Razaq, D. Sun, Y. Xin, Q. Li, T. Huang, L. Zheng, Z. Zhang, Y. Huang, *Nanotechnology* **2018**, *29*, 295401; d) Y. Wu, X. Zhu, P. Li, T. Zhang, M. Li, J. Deng, Y. Huang, P. Ding, S. Wang, R. Zhang, J. Lu, G. Lu, Y. Li, Y. Li, *Nano Energy* **2019**, *59*, 636–643; e) R. Razaq, N. Zhang, Y. Xin, Q. Li, J. Wang, Z. Zhang, *EcoMat* DOI 10.1002/eom2.12020.
[21] a) Z. Cui, C. Zu, W. Zhou, A. Manthiram, J. B. Goodenough, *Adv. Mater.* 2016, 28, 6926; b) Z. Sun, J. Zhang, L. Yin, G. Hu, R. Fang, H. M. Cheng, F. Li, *Nat. Commun.* **2017**, *8*, 14627.
[22] W. G. Lim, C. Jo, A. Cho, J. Hwang, S. Kim, J. W. Han, J. Lee, *Adv. Mater.* **2019**, *31*, 1806547.
[23] M. Zhao, H. J. Peng, B. Q. Li, X. Chen, J. Xie, X. Liu, Q. Zhang, J. Q. Huang, *Angew. Chem. Int. Ed.* **2020**, *59*, 9011.
[24] a) T. Chen, Z. Zhang, B. Cheng, R. Chen, Y. Hu, L. Ma, G. Zhu, J. Liu, Z. Jin, *J. Am. Chem. Soc.* **2017**, *139*, 12710–12715; b) H. Zhang, M. Zou, W. Zhao, Y. Wang, Y. Chen, Y. Wu, L. Dai, A. Cao, *ACS Nano* **2019**, *13*, 3982–3991; c) X. Yang, X. Gao, Q. Sun, S. P. Jand, Y. Yu, Y. Zhao, X. Li, K. Adair, L. Y. Kuo, J. Rohrer, J. Liang, X. Lin, M. N. Banis, Y. Hu, H. Zhang, X. Li, R. Li, H. Zhang, P. Kaghazchi, T. K. Sham, X. Sun, *Adv. Mater.* **2019**, *31*, 1901220.
[25] Z. Yuan, H. J. Peng, T. Z. Hou, J. Q. Huang, C. M. Chen, D. W. Wang, X. B. Cheng, F. Wei, Q. Zhang, *Nano Lett.* **2016**, *16*, 519–527.
[26] R. Razaq, D. Sun, J. Wang, Y. Xin, G. Abbas, J. Zhang, Q. Li, T. Huang, Z. Zhang, Y. Huang, *J. Power Sources* **2019**, *414*, 453–459.
[27] M. Chen, W. Xu, S. Jamil, S. Jiang, C. Huang, X. Wang, Y. Wang, H. Shu, K. Xiang, P. Zeng, *Small* **2018**, *14*, 1803134.
[28] B.-Q. Li, H.-J. Peng, X. Chen, S.-Y. Zhang, J. Xie, C.-X. Zhao, Q. Zhang, *CCS Chem.* **2019**, *1*, 128–137.
[29] P. T. Dirlam, J. Park, A. G. Simmonds, K. Domanik, C. B. Arrington, J. L. Schaefer, V. P. Oleshko, T. S. Kleine, K. Char, R. S. Glass, C. L. Soles, C. Kim, N. Pinna, Y. E. Sung, J. Pyun, *ACS Appl. Mater. Interfaces* **2016**, *8*, 13437–13848.
[30] H. Lin, L. Yang, X. Jiang, G. Li, T. Zhang, Q. Yao, G. W. Zheng, J. Y. Lee, *Energy Environ. Sci.* **2017**, *10*, 1476–1486.
[31] G. Liu, A. W. Robertson, M. M.-J. Li, W. C. H. Kuo, M. T. Darby, M. H. Muhieddine, Y.-C. Lin, K. Suenaga, M. Stamatakis, J. H. Warner, S. C. E. Tsang, *Nat. Chem.* **2017**,*9*, 810–816.
[32] X. Yang, Q. Li, E. Lu, Z. Wang, X. Gong, Z. Yu, Y. Guo, L. Wang, Y. Guo, W. Zhan, J. Zhang, S. Dai, *Nat. Commun.* **2019**, *10*, 1611.
[33] W. Xue, Z. Shi, L. Suo, C. Wang, Z. Wang, H. Wang, K. P. So, A. Maurano, D. Yu, Y. Chen, L. Qie, Z. Zhu, G. Xu, J. Kong, J. Li, *Nat. Energy* **2019**, *4*, 374–382.
[34] I. S. Amiinu, Z. Pu, X. Liu, K. A. Owusu, H. G. R. Monestel, F. O. Boakye, H. Zhang, S. Mu, *Adv. Funct. Mater.* **2017**, *27*, 1702300.

[35] X. Tang, Z. Sun, H. Yang, H. Fang, F. Wei, H.-M. Cheng, S. Zhuo, F. Li, *J. Energy Chem.* **2019**, *31*, 119.
[36] X. Huang, J. Tang, B. Luo, R. Knibbe, T. Lin, H. Hu, M. Rana, Y. Hu, X. Zhu, Q. Gu, D. Wang, L. Wang, *Adv. Energy Mater.* **2019**, *9*, 1901872.
[37] X. Xie, T. Makaryan, M. Zhao, K. L. Van Aken, Y. Gogotsi, G. Wang, *Adv. Energy Mater.* **2016**, *6*, 1502161.
[38] Y. Li, P. Xu, G. Chen, J. Mou, S. Xue, K. Li, F. Zheng, Q. Dong, J. Hu, C. Yang, M. Liu, *Chem. Eng. J.* **2020**, *380*, 122595.
[39] Z. Zeng, W. Li, Q. Wang, X. Liu, *Adv. Sci.* **2019**, *6*, 1900711.
[40] M. Zhao, H. J. Peng, Z. W. Zhang, B. Q. Li, X. Chen, J. Xie, X. Chen, J. Y. Wei, Q. Zhang, J. Q. Huang, *Angew. Chem. Int. Ed.* **2019**, *58*, 3779.
[41] Y. Song, W. Zhao, X. Zhu, L. Zhang, Q. Li, F. Ding, Z. Liu, J. Sun, *ACS Appl. Mater. Interfaces* **2018**, *10*, 15733–15741.
[42] C. Ye, D. Chao, J. Shan, H. Li, K. Davey, S.-Z. Qiao, *Matter* **2020**, *2*, 323–344.

Submitted: April 27, 2020
Accepted: June 22, 2020